TUDelft

Delft University of Technology

A numerical method for reorientation of rotating tidally deformed viscoelastic bodies

Hu, H.; van der Wal, W.; Vermeersen, L. L A

Important note
To cite this publication, please use the final published version (if applicable).
Please check the document version above.

A numerical method for reorientation of rotating tidally deformed viscoelastic bodies

H. Hu[1], W. van der Wal[1], and L. L. A. Vermeersen[1]

[1]Department of Aerospace Engineering, Delft University of Technology, Delft, Netherlands

Abstract Existing approaches for simulating the true polar wander (TPW) of a viscoelastic body can be divided into three categories: (i) a linear dynamic approach which uses the linearized Liouville equation (e.g., Wu and Peltier (1984) and Mitrovica et al. (2005)); (ii) a nonlinear dynamic approach which is based on the quasi-fluid approximation (e.g., Sabadini and Peltier (1981), Ricard et al. (1993), and Cambiotti et al. (2011)); and (iii) a long-term limit approach which only considers the fluid limit of a reorientation (e.g., Matsuyama and Nimmo (2007)). Several limitations of these approaches have not been studied: the range for which the linear approach is accurate, the validity of the quasi-fluid approximation, and the dynamic solution for TPW of a tidally deformed rotating body. We establish a numerical procedure which is able to determine the large-angle reorientation of a viscoelastic celestial body that can be both centrifugally and tidally deformed. We show that the linear approach leads to significant errors for loadings near the poles or the equator. Second, we show that slow relaxation modes can have a significant effect on large-angle TPW of Earth or other planets. Finally, we show that reorientation of a tidally deformed body driven by a positive mass anomaly near the poles has a preference for rotating around the tidal axis instead of toward it. At a tidally deformed body which does not have a remnant bulge, positive mass anomalies are more likely to be found near the equator and the plane perpendicular to the tidal axis, while negative mass anomalies tend to be near the great circle that contains the tidal and rotational axes.

1. Introduction

True polar wander (TPW), the nonperiodical secular part of the displacement of the rotation axis with respect to surface topography or internal signatures, has been proposed to be the cause of many geographic features on various planets and moons (e.g., Mars [*Schultz and Lutz*, 1988], Venus [*Malcuit*, 2014], Enceladus [*Nimmo and Pappalardo*, 2006], and Europa [*Ojakangas and Stevenson*, 1989]). The theoretical study of TPW can be dated back to *Gold* [1955] who introduced the modern concept and general mechanism of TPW. After the development of the normal mode method [*Farrell*, 1972], the Liouville equation could be solved semianalytically [*Sabadini and Peltier*, 1981] for a viscoelastic multilayer model to arrive at the dynamic solution of TPW. Early studies focused on the speed of present-day TPW and small angular change, so a linear approach, which applies the linearized form of the Liouville equation [*Munk and MacDonald*, 1960], was adopted to calculate TPW when the rotational axis is not too far away from the initial position [*Nakiboglu and Lambeck*, 1980; *Sabadini and Peltier*, 1981; *Wu and Peltier*, 1984]. In order to deal with the long-term rotational variation of Earth which may include large angular TPW, nonlinear methods have been developed, but they adopt the quasi-fluid approximation which assumes that the variation of the driving force for TPW is much slower compared to the characteristic viscous relaxation. Mathematically, the quasi-fluid approximation is a first-order approximation in the Taylor expansion of the tidal Love number [*Spada et al.*, 1992; *Ricard et al.*, 1993; *Cambiotti et al.*, 2011]. Thus, these semianalytical solutions have several limitations. Specifically, the approximations which have been adopted in the development of the methods have not been quantitatively tested. They will be discussed in the following.

First, although some later studies solve the Liouville equation in different ways such as with a finite difference method [*Nakada*, 2002; *Mitrovica et al.*, 2005], the linearized form of the Liouville equation is still used and there is a limit for the allowed range of TPW in order for the error to remain small. In order to show the limit of the linear method, *Sabadini and Peltier* [1981], within the frame of the quasi-fluid approximation, carried out a comparison between the nonlinear scheme and the linear scheme, arriving at the conclusion that the linear method is valid for TPW of about 10° from the initial position of the rotation pole. The linearized form of
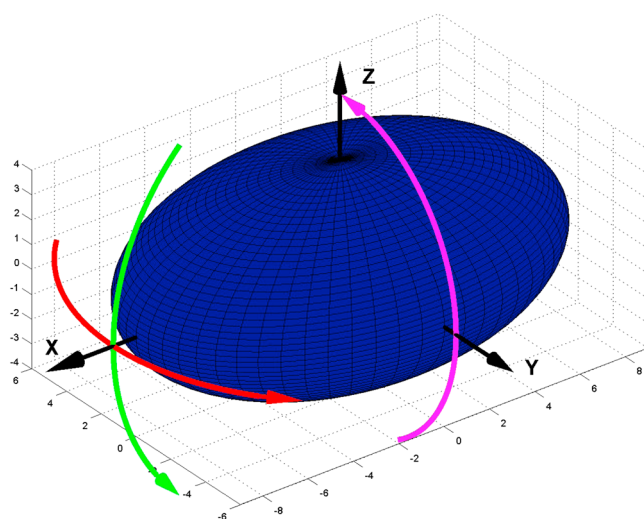
Figure 1. The bulge-fixed coordinate system in a tidally deformed rotation body. The *X* axis is the tidal axis and points toward the central body. The *Z* axis is the rotation axis, and the *Y* axis completes a right-handed coordinate system. The colored arrows show three reorientations around the axes, which will be labeled as *X*, *Y*, and *Z* reorientation.

the Liouville equation is derived in the body-fixed frame where the rotational axis coincides with the vertical axis in the beginning [*Munk and MacDonald*, 1960]. Since the loading (the inertia tensor representing the geophysical process on the solid model) is also defined in the body-fixed fame, the linear theory actually also assumes that the relative location of the loading with respect to the rotational axis does not change during TPW. This assumption can lead to a large error for certain locations of the loading. For instance, when a point mass is located near the poles or equator, the effect of a change in colatitude of the point mass is relatively large. As a result, the linear methods should have a much smaller applicable range for loadings near the pole or equator. Currently, no study gives the expected error as a function of the angle of TPW and the position of the load when the linearized form of the Liouville equation is applied.

Second, the nonlinear approach is currently the only general way to calculate large-angle TPW. As a result, the effect of the quasi-fluid approximation, which has been the fundamental assumption of many previous studies [*Spada et al.*, 1992, 1996; *Ricard et al.*, 1993; *Harada*, 2012; *Chan et al.*, 2014], has not been tested. So it is not clear what the effect is of taking the quasi-fluid approximation and ignoring the effects of the slow modes (such as the M1 and M2 modes for Earth) on the path of TPW.

Third, a rotating tidally deformed body can be very difficult to deal with by current linear or nonlinear rotation theory. As shown in Figure 1, there are three different reorientations of a tidally deformed body, while there is only one type of the reorientation when only a centrifugal force is applied. As a result, the complete description of the reorientation of a tidally deformed rotating body consists of the polar wander of both the rotational and tidal axes. We are not aware of other methods which solve the Liouville equation to give a time-dependent solution for the reorientation of a rotating tidally deformed viscoelastic body. Most studies concerning TPW of a tidally deformed body only focus on the fluid limit of the viscoelastic response which gives the final position of the rotational or tidal axis [*Willemann*, 1984; *Matsuyama and Nimmo*, 2007]. In practice, it is difficult to know if the TPW or reorientation has already finished and the rotational or tidal axis are in their final position. This limits the application of methods which only calculate the final position and not the full reorientation path. More importantly, since these methods do not provide dynamic solutions, we do not have a clear insight on how the reorientation is accomplished. Studies which concern the direction of polar wander of tidally deformed bodies driven by either a positive mass anomaly such as ice caps on Triton [*Rubincam*, 2003] or a negative mass anomaly such as a diapirism-induced low-density area on Enceladus [*Matsuyama and Nimmo*, 2007; *Nimmo and Pappalardo*, 2006] suggest that the polar motion is directly targeting its end position. However, these suggestions are not tested in these papers because a theory for combined centrifugally and tidally induced TPW is lacking.

Considering all above mentioned problems and the difficulty of solving the Liouville equation analytically, we create a numerical model to tackle these problems. Another advantage of adopting a numerical approach is that the normal mode method, which is the foundation of all above mentioned dynamic rotation methods, can only be applied for a radially symmetric model, while many planets and moons can have considerable lateral heterogeneity, for example, Mars [*Šrámek and Zhong*, 2012] or Enceladus [*Nimmo and Pappalardo*, 2006].

The purpose of this paper is to establish a general numerical method which can determine the secular part of the rotational variation of a centrifugally and tidally deformed viscoelastic body. With the help of this method we aim to answer the following questions:

1. What is the effect of assuming that the load is stationary relative to the rotational axis in the linear method?
2. What is the effect of the quasi-fluid approximation for the TPW path of a planetary model?
3. How is the reorientation of a tidally deformed body driven by a certain mass anomaly accomplished?

It is important to note that we only consider pure viscoelastic bodies without a remnant bulge in this study. For some planets such as Earth, during the early stages of their formation, the outer layer cools down in an ellipsoidal shape and becomes fixed. The existence of such a bulge can have a significant effect on the behavior of TPW. For the case of Earth and some other celestial bodies, this issue has been intensively studied during the past decades [*Willemann*, 1984; *Mitrovica et al.*, 2005; *Matsuyama and Nimmo*, 2007; *Cambiotti et al.*, 2010; *Mitrovica and Wahr*, 2011; *Chan et al.*, 2014]. The existence of a remnant bulge would have two effects. First, during the TPW, since the stress in the outer layer cannot relax as the rest of the viscoelastic parts, the remaining stress in this layer would prevent the equatorial bulge to fully adjust into the vertical position to the rotational axis. Because of this, a positive anomaly, for instance, will not reach the equator as for the case of a pure viscoelastic body, as is demonstrated in *Mitrovica et al.* [2005, Figure 14]. Second, when the TPW is finished or during the TPW, if the mass anomaly which causes the TPW is removed from the body, the stress in the outer layer would try to restore the shape of the body back into its initial form before the TPW starts, so the rotational axis would go back to its initial position. This is different from the case of a purely viscoelastic body in which the rotational axis is expected to retain its final position when the mass anomaly is removed. As a result, the study of TPW on models with such an elastic layer is significant. However, the numerical procedures and the validation of such models are beyond the scope and purpose of this paper. So in this paper, only models without a remnant bulge are considered.

The content is organized as follows: section 2 shows how the change in the inertia tensor can be obtained by a finite element modeling (FEM). Section 3 presents a numerical method for solving the Liouville equation. After validating our numerical results with previous semianalytical methods, we test the above mentioned assumptions. Finally, section 4 presents a method to calculate the reorientation of a tidally deformed rotating viscoelastic body and shows the cases of a body driven by a positive and negative mass anomaly respectively. This paper only focuses on the laterally homogeneous case.

2. Finite Element Approach for Calculating the Change in the Moment of Inertia

The Liouville equation gives the general dynamics of a rotational body that can deform. When no external torque is applied, it reads [*Sabadini and Vermeersen*, 2004]

$$\frac{d}{dt}(\mathbf{I} \cdot \boldsymbol{\omega}) + \boldsymbol{\omega} \times \mathbf{I} \cdot \boldsymbol{\omega} = 0 \tag{1}$$

where **I** is the inertia tensor and $\boldsymbol{\omega}$ is the rotational vector. Both values are defined in a body-fixed coordinate system. In order to solve this equation, information about the change in the inertia tensor must be given. When the moments of inertia are perturbed by a geophysical process for a centrifugally deformed body without tidal deformation, the rotational axis shifts, and the resulting change in the centrifugal force also deforms the body. Analytically, given a rotational vector as $\boldsymbol{\omega} = \Omega(\omega_1, \omega_2, \omega_3)^T$, where Ω is the angular speed of the rotation and $(\omega_1, \omega_2, \omega_3)^T$ is a unit vector which represents the direction of the rotation, the total moment of inertia attributable to such process is given by (similar to equation 2 in *Ricard et al.* [1993])

$$I_{ij}(t) = I\delta_{ij} + \frac{k^T(t)a^5}{3G} * \left(\Omega^2 \left[\omega_i(t)\omega_j(t) - \frac{1}{3}\delta_{ij} \right] \right) + [\delta(t) + k^L(t)] * C_{ij}(t) \tag{2}$$

where I is the principle moment of inertia of the unloaded laterally homogeneous spherical body and G and a are the gravitational constant and the radius of the planet, respectively. $k^T(t)$ and $k^L(t)$ are the degree 2 tidal Love number and load Love number, respectively. The $*$ denotes convolution in the time domain. C_{ij} represents the change in the moments and products of inertia without considering the dynamic deformation. These values trigger the polar wander. The second and third terms in equation (2) represent the changes which derive from the perturbed centrifugal force and from the mass redistribution induced by the original load,
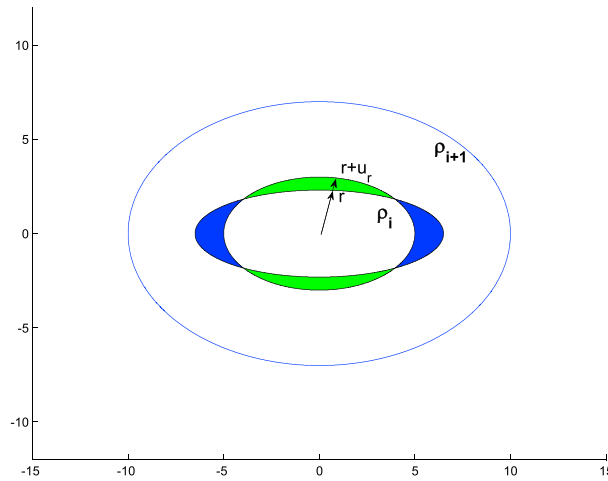
Figure 2. Deformation of a boundary layer whose radius changes from r to $r + u_r$. The densities inside and outside of the layer are ρ_i and ρ_{i+1}, respectively.

respectively. The use of Love numbers limits the simulation to the case of a laterally homogeneous model, and thus, we also seek a numerical method as an alternative for equation (2) to calculate the change in the inertia tensor. This will be the foundation for dealing with heterogeneous cases in our second paper.

In order to obtain the change in the inertia tensor, we need to know the deformation of the body for which we can use FEM. This part is mainly based on the method of *Wu* [2004]. One of the problems of applying FEM to calculate the viscoelastic response of a 3-D celestial body is the effect of gravitation which is dependent on the deformation itself. In *Wu* [2004], the deformation is first determined by assuming the perturbed potential is zero, and the result from FEM is used to calculate the perturbed potential. The potential is applied to the model again and iteration continues until the result converges. We develop a finite element (FE) model with the commercial package Abaqus version 6.13 in which the average grid size for the Earth model is chosen to be around 400 km and linear brick elements are used. With the information of the deformation the change in the inertia tensor is also calculated numerically after the result from FEM converges. In the FE model, the Poisson ratio of the planet model can be set to that of a compressible material, but the effects of a change in density on gravity and inertia are not taken into account. Hence, our method does not include the full effect of compressibility but only material compressibility (similar to, e.g., *Wang et al.* [2008]). Since we ignore the density changes, when the deformation is small, only the radial displacement for each layer is required for calculating the change in the moment of inertia, which is shown in the following method. As we can see in Figure 2, the deformation changes the shapes of the boundaries which switches the density of certain parts: for the shaded area in Figure 2, the density of the green parts changes from ρ_{i+1} to ρ_i and the density of blue parts changes from ρ_i to ρ_{i+1}. As a result, for a model which contains N layers, at the pth internal boundary, the change in the inertia tensor is calculated as

$$\Delta I_{ij,p} = \int_{\Delta V} (\rho_{p+1} - \rho_p)(r_k r_k \delta_{ij} - r_i r_j) dV$$

$$\simeq \int_S (\rho_{p+1} - \rho_p)(r_k r_k \delta_{ij} - r_i r_j) u_r dS, \quad p = 0, 1, 2, \dots, N-1$$

and at the surface

$$\Delta I_{ij,N} = \int_S (\rho_N)(r_k r_k \delta_{ij} - r_i r_j) u_r dS \tag{3}$$

Here ΔV is the perturbed volume which contains the above mentioned density switch and S is the complete interface or the surface. The complete change of the inertial tensor is given by the sum of the changes at all interfaces and at the surface:

$$\Delta I_{ij} = \sum_{p=0}^{N} \Delta I_{ij,p} \tag{4}$$

Table 1. Properties of the Two-Layer Earth Model

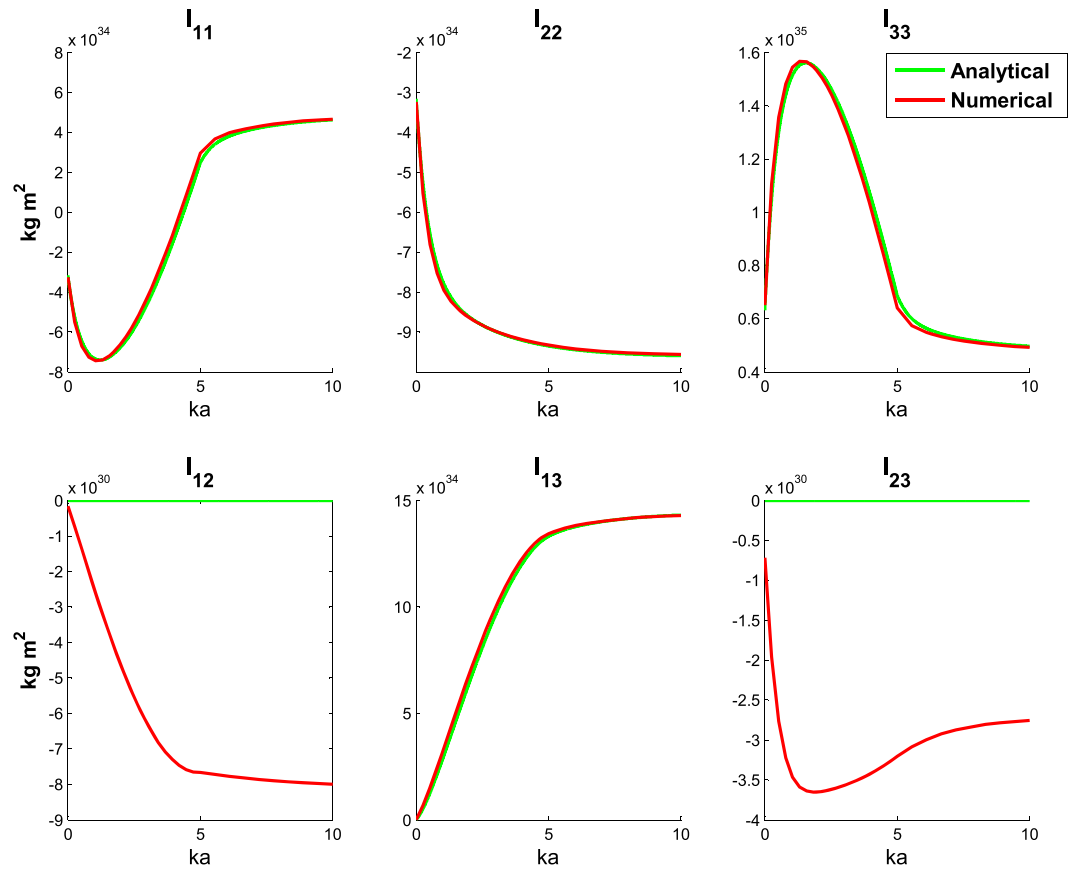| Layer	Outer Radius (km)	Density (kg m^{-3})	Shear Modulus (Pa)	Viscosity (Pa s)
Mantle	6,371	4,448	1.7364×10^{11}	1×10^{21}
Core	3,480	10,977	0	0

Figure 3. Change in the moment of inertia for a two-layer Earth model with the rotation axis linearly drifting from 0 to 45° colatitude in the *x-z* plane in 5000 years.

We validate our FE model by calculating the change in the inertia tensor of a two-layer Earth model (Table 1) which is forced by a varying centrifugal force.

We apply the centrifugal force to an initially unloaded model and let the rotational axis move toward the equator with a constant speed of 45° in 5000 years. The change in the moment of inertia for this case can be calculated by equation (2) with $C_{ij}(t) = 0$. The comparison between the semianalytical and FEM results is given in Figure 3. For the nonzero components I_{11}, I_{22}, I_{33}, and I_{13}, the numerical results show very good agreement with the semianalytical results. FEM results of I_{12} and I_{23} are also nonzero while they should be theoretically zero. However, the numerical results of these two values are about 4 orders of magnitude smaller than the other four components in the inertia tensor. Thus, these values result in a numerical error which is around 0.1% for our configuration of a mesh with an average grid size of 400 km for the Earth model.

As will be shown in the next section in the linearized Liouville equation and algorithm 2, the accuracy of the TPW is controlled by four terms which are combinations of components of the inertia tensor and the angular speed in a coordinate system whose *z* axis coincides with the rotational axis: $\frac{\Delta I_{13}(t)}{C-A}$, $\frac{\Delta I_{23}(t)}{C-B}$ and $\frac{C\Delta \dot{I}_{13}(t)}{\Omega(C-A)(C-B)}$, $\frac{C\Delta \dot{I}_{23}(t)}{\Omega(C-A)(C-B)}$. In order to show that the change in the moment of inertia obtained from FEM is accurate enough for calculating TPW, we compare both the analytical and numerical values of these four terms for a given TPW history. As shown in Figure 4, the theoretical nonzero terms $\frac{\Delta I_{13}(t)}{C-A}$ and $\frac{C\Delta \dot{I}_{13}(t)}{\Omega(C-A)(C-B)}$ show very good agreement. For a grid size of 300 km, the $\frac{\Delta I_{13}(t)}{C-A}$ and $\frac{C\Delta \dot{I}_{13}(t)}{\Omega(C-A)(C-B)}$ terms have less than 0.5% error level. We see again that two theoretical zero components are at least 4 orders of magnitude smaller than the nonzero components. It was found that in order to get results close to the analytic result which is based on Maxwell rheology, in Abaqus, a "Viscoelastic" option needs to be used. The viscoelastic setting in Abaqus uses the Prony series which is a general scheme that encompasses a simple Maxwell rheology. We show this issue in Appendix A.
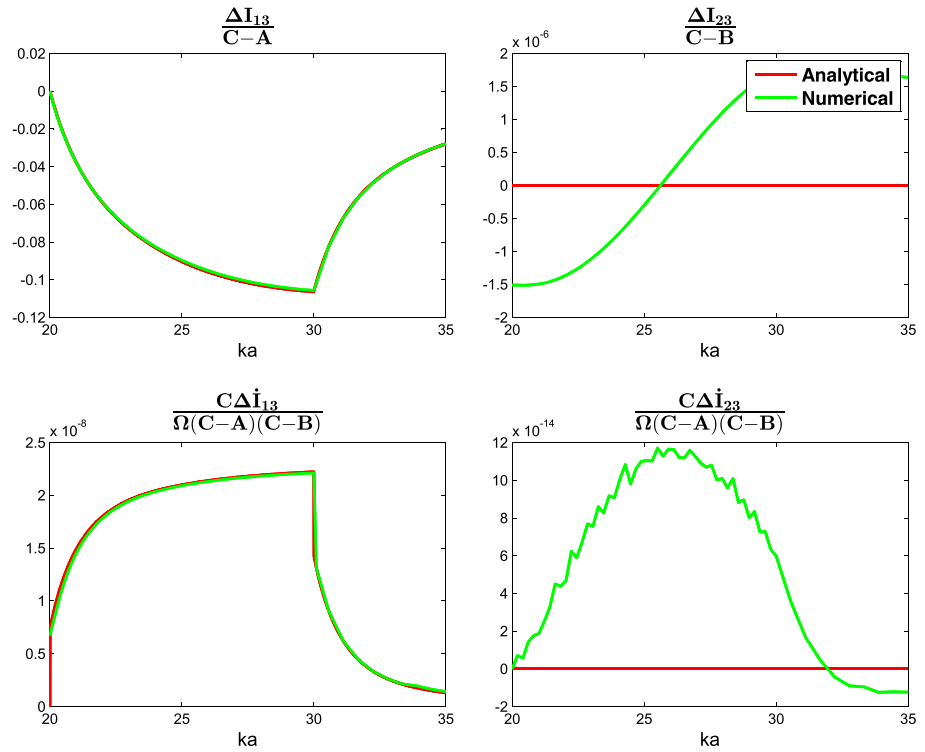
Figure 4. Values of four terms for a SG6 Earth model with the rotation axis linearly drifting from 0 to 45 degree colatitude in the x-z plane in 10 thousand years after the centrifugal force is applied to the spherical model for 20 thousand years.

3. Numerical Solutions of Liouville Equation

With the information about the change in the inertia tensor obtained either by equation (2) or FEM, the Liouville equation can be solved numerically. Cases with small angular change, to which linear theory can be directly applied, and large angular change will be dealt with separately. We validate our numerical methods by comparing the results with semianalytical linear [*Wu and Peltier*, 1984] and nonlinear [*Ricard et al.*, 1993] methods with the same assumptions. After that, we test the validity of the assumptions made in these methods.

3.1. Small-Angle Polar Wander

Considering that we want to deal with lateral heterogeneity in paper II and tidally deformed bodies, we first need to derive a more general form of the linearized Liouville equation. The procedure is similar to that given on page 104 of *Sabadini and Vermeersen* [2004].

In equation (1), when assuming that changes in **I** are small, the perturbed inertia tensor can be written as

$$\mathbf{I} = \begin{pmatrix} A + \Delta I_{11} & \Delta I_{12} & \Delta I_{13} \\ \Delta I_{21} & B + \Delta I_{22} & \Delta I_{23} \\ \Delta I_{31} & \Delta I_{32} & C + \Delta I_{33} \end{pmatrix} \tag{5}$$

Here A, B, and C denote the moments of inertia of the rotational body for the equatorial principal axes and polar principal axis. We do not assume $A = B$ as in *Sabadini and Vermeersen* [2004]. We define the perturbed vector of the rotation as

$$\boldsymbol{\omega} = \Omega(m_1, m_2, 1 + m_3)^T \tag{6}$$

where Ω is the angular speed of the rotation and m_i, $i = 1, 2, 3$ are small values with m_1 and m_2 representing the TPW and m_3 the change in the length of the day (LOD). By omitting the products of the small quantities m_i and ΔI_{ij}, we have

$$\mathbf{I} \cdot \boldsymbol{\omega} \approx \begin{pmatrix} A\Omega m_1 + \Omega\Delta I_{13} \\ B\Omega m_2 + \Omega\Delta I_{23} \\ C\Omega + Cm_3\Omega + \Delta I_{33}\Omega \end{pmatrix} \tag{7}$$

$$\boldsymbol{\omega} \times (\mathbf{I} \cdot \boldsymbol{\omega}) \approx \begin{pmatrix} -Bm_2\Omega^2 + Cm_2\Omega^2 - \Delta I_{23}\Omega^2 \\ Am_1\Omega^2 - Cm_1\Omega^2 + \Delta I_{13}\Omega^2 \\ 0 \end{pmatrix} \tag{8}$$

Substituting equations (7) and (8) into equation (1) we have

$$\dot{m}_1 = -\frac{C-B}{A}\Omega m_2 + \frac{\Omega}{A}\Delta I_{23} - \frac{\Delta \dot{I}_{13}}{A} \tag{9a}$$

$$\dot{m}_2 = \frac{C-A}{B}\Omega m_1 - \frac{\Omega}{B}\Delta I_{13} - \frac{\Delta \dot{I}_{23}}{B} \tag{9b}$$

$$\dot{m}_3 = -\frac{\Delta \dot{I}_{33}}{C} \tag{9c}$$

Note that now we cannot define the Eulerian free precession frequency as $\sigma_r = \frac{C-A}{A}\Omega$ to further combine these equations. Equation (9) gives the rotational dynamics of a triaxial body for a small perturbation which has been previously studied by *Hinderer et al.* [1982] and *Matsuyama et al.* [2010] for the case of Earth. *Matsuyama et al.* [2010] made the assumptions that the time scale of the loading is much longer than both the period of rotation and the Euler wobble periods. Based on these assumptions, the derivatives on both side of equation (9) are ignored. The same procedure is also used in *Sabadini and Vermeersen* [2004]. These assumptions might be true for Earth but not for some slow rotating bodies like Venus. In order to establish a more general method, we cannot directly ignore these derivative terms. Instead, we take advantage of the fact that numerically, the TPW is calculated stepwise and deal with equation (9) as follows: In each step of the numerical integration, we assume that the size of the step is small enough so that the change in the inertia tensor can be treated as linear, which gives

$$\Delta I_{13}(t) = a_1 + b_1 t \tag{10a}$$

$$\Delta I_{23}(t) = a_2 + b_2 t \tag{10b}$$

After substituting (10) into (9), m_1, m_2 can be solved analytically. The results contain both secular terms and periodic terms, which represent the TPW and the Chandler wobble, respectively. We ignore the periodical terms and obtain

$$m_1(t) = \frac{\Delta I_{13}(t)}{C-A} + \frac{C\Delta \dot{I}_{23}(t)}{\Omega(C-A)(C-B)} \tag{11a}$$

$$m_2(t) = \frac{\Delta I_{23}(t)}{C-B} - \frac{C\Delta \dot{I}_{13}(t)}{\Omega(C-A)(C-B)} \tag{11b}$$

$$m_3(t) = -\frac{\Delta I_{33}}{C} \tag{11c}$$

Besides the A and B terms, the equations also contain the derivatives of the elements of the inertia tensor. When only the centrifugal force is considered for a laterally homogeneous model, $(C - A)/C = (C - B)/C$ represents the flattening of the model and the magnitude of $(C - A)/C$ is proportional to the square of the rotational rate Ω^2. As a result, the magnitudes of the second terms on the right side become significantly larger for slowly rotating bodies such as Venus. When the magnitude of the second terms on the right side becomes comparable to that of the first terms, it results in the phenomenon of so-called mega wobble [*Spada et al.*, 1996; *Sabadini and Vermeersen*, 2004] as shown on the right Figure 5a. For most of the bodies in the solar system including Earth, long-term TPW acts as in Figure 5b. In this case the part which contains the derivatives
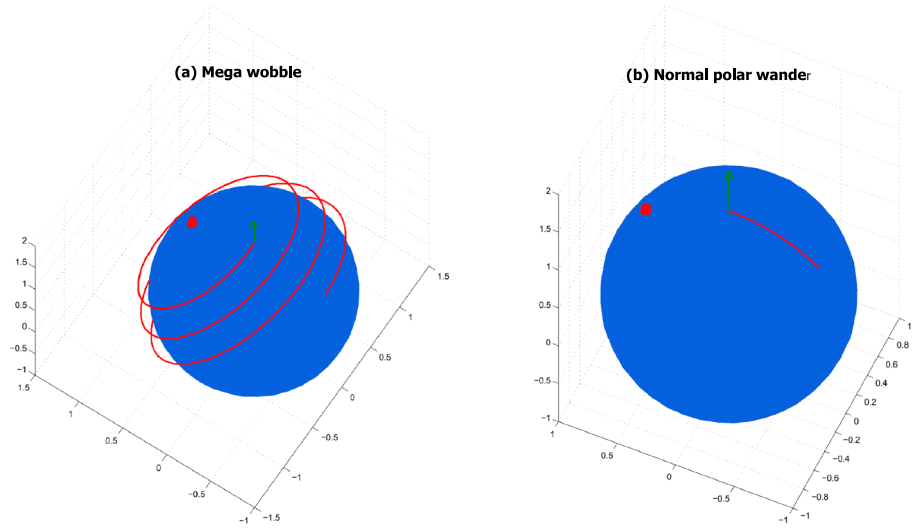
Figure 5. Two types of polar wander path. The green arrow is the initial position of the rotational axis and the red dot is the point mass load.

of the changes in the inertia tensor is small and the path of TPW driven by a point mass is almost along the great circle of the body. So if we place a point mass load in the *x-z* plane, the TPW can be almost completely described by the value m_1.

Since we study the TPW of bodies in the hydrostatic state, the centrifugal force needs to be applied for a certain length of time T_0 until the model can be considered to have reached its equilibrium. For laterally homogeneous models, the choice of T_0 can be derived from the time history of the tidal Love number. We choose T_0 to be the time at which the tidal Love number reaches more than 99.95% of the fluid tidal Love number:

$$k^T(T_0) > 99.95\% \, k_f^T \tag{12}$$

Here k_f^T is the fluid tidal love number. For the two-layer Earth model of Table 1 it follows that $T_0 = 15$ ka. In the FE model, we apply a centrifugal force at its original rotational axis for T_0 before we start to apply the algorithm to calculate the path of TPW. If equation (2) is used, then we have

$$\boldsymbol{\omega}(t) = (0, 0, \Omega) \quad \text{for} \quad 0 \leq t \leq T_0 \tag{13}$$

where Ω is the angular velocity of the body. For a centrifugally deformed body triggered by a mass anomaly with inertia tensor $\Delta \mathbf{I}_L$, the algorithm for calculating the small-angle polar wander and LOD $m = (m_1, m_2, m_3)$ is given as follows.

Algorithm 1

1. Assume that the step *i* starts at time t_i with the rotational axis being located at $\boldsymbol{\omega}^i = \Omega^i(m_1^i, m_2^i, 1 + m_3^i)$ and ends at time t_{i+1} with the rotational axis at $\boldsymbol{\omega}^{i+1}$. For the first iteration we assume that the rotation axis does not change: $\boldsymbol{\omega}^{i+1} = \boldsymbol{\omega}^i$.
2. For a laterally homogeneous model we use equation (2) for calculating the change in the inertia tensor. In equation (2), set $C_{ij}(t) = \Delta I_{L\_ij}$ and let

$$\boldsymbol{\omega}(t) = \boldsymbol{\omega}^i + \frac{t_i - t}{t_i - t_{i+1}} \boldsymbol{\omega}^{i+1} \quad \text{for} \quad t_i \leq t \leq t_{i+1} \tag{14}$$

then the result of equation (2) can directly give the total change in the inertia tensor $\Delta \mathbf{I}$ and its derivative $\Delta \dot{\mathbf{I}}$. For a laterally heterogeneous model we use FEM to obtain the inertia tensor. We change the centrifugal potential from its initial direction along $\boldsymbol{\omega}^i$ at t_i linearly to its new direction of $\boldsymbol{\omega}^{i+1}$ at t_{i+1} in the FEM and calculate the change in the inertia tensor $\Delta \mathbf{I}_D$ and its derivative $\Delta \dot{\mathbf{I}}_D$ due to centrifugal deformation and

Table 2. Properties of the Viscoelastic Earth Model SG6

Layer	Outer Radius (km)	Density (kg m^{-3})	Shear Modulus (Pa)	Viscosity (Pa s)
Lithosphere	6,371	4,120	0.73×10^{11}	∞
Upper mantle	6,271	4,120	0.95×10^{11}	0.6×10^{21}
Transition zone	5,950	4,220	1.10×10^{11}	0.6×10^{21}
Shallow lower mantle	5,700	4,508	2.00×10^{11}	1.6×10^{21}
Deeper lower mantle	5,040	4,508	2.00×10^{11}	3×10^{21}
Core	3,480	10,925	0	0

surface load by equation (4). The total change in the inertia tensor is the sum of that due to the deformation and the tensor of the initial load: $\Delta \mathbf{I} = \Delta \mathbf{I}_D + \Delta \mathbf{I}_L$, $\Delta \dot{\mathbf{I}} = \Delta \dot{\mathbf{I}}_D + \Delta \dot{\mathbf{I}}_L$.

3. Substitute $\Delta \mathbf{I}$ and $\Delta \dot{\mathbf{I}}$ into equation (11) and obtain the updated ω^{i+1}. This value is fed back into step 2 until the result converges.

The small-angle numerical results are compared with results from the linear semianalytical method of *Wu and Peltier* [1984]. In that paper, the Chandler wobble is filtered out by assuming that all rotational modes have a much longer relaxation time than the Chandler wobble. By taking $|s| \ll \sigma_0$, where s and σ_0 are the Laplace frequency and Eulerian free precession frequency, respectively, the imaginary, harmonic part of the fundamental mantle mode (M0) which contributes most to the Chandler wobble, is omitted. It has been proven that the elastic term of equation (79) in *Wu and Peltier* [1984] is a highly accurate approximation of the effect on TPW of the real part of the M0 mode [*Vermeersen and Sabadini*, 1996; *Peltier and Jiang*, 1996]. So for small angular motion, since the method stated in *Wu and Peltier* [1984] contains the effects of all modes, we expect that it gives an accurate prediction of the TPW on a layered viscoelastic model against which our method can be benchmarked. We test our method both with the two-layer Earth model (Table 1) and the six-layer Earth model SG6 as defined in Table 2. We calculate the corresponding Love number of this model by setting the viscosity of the lithosphere to an extremely high value but exclude the slowest mode generated by this layer. This scenario corresponds to the situation where the elastic layer exists before the centrifugal potential is applied to the spherical Earth, as demonstrated in Figure 14 of [*Mitrovica et al.*, 2005] as case B. Of course this situation does not correspond to the real Earth (cases C and D in the same figure) which has a remnant bulge. However, as mentioned in the introduction, the purpose here is method development and validation, and we leave the effect of a remnant bulge in our method to future work. The models are driven by a constant point mass of 2×10^{19} kg which is attached to the surface at 45° colatitude. We assume
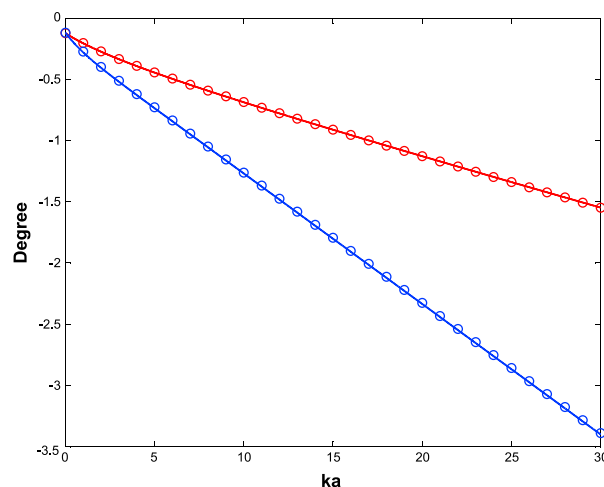
that the point mass is stationary at the surface, so in equation (2) $k_L = 0$. For the SG6 model, the initial time T_0 for which the centrifugal force needs to be applied is chosen to be 4 million years according to equation (12). The numerical results for both models agree very well with the prediction of *Wu and Peltier* [1984], see Figure 6. From this figure, we can also see the effect of the delayed viscous adjustment of the rotational bulge. This stabilization is larger for layers with higher viscosity, and this is why TPW of SG6 model driven by the same anomaly is slower.

Usually 7–8 iterations in each step are necessary for the use of equation (2), and 9–10 for FEM with equation (4) are required to achieve an accuracy of 0.1%. The required number of iterations is reduced for smaller step sizes.

Figure 6. The polar wander path in the *x-z* plane of the two-layer (blue) and SG6 (red) Earth models triggered by a mass anomaly of 2×10^{19} kg attached at 45° colatitude in the *x-z* plane. Lines show the results with semianalytical method of *Wu and Peltier* [1984], and circles represent our numerical ones.

The agreement of our numerical method and the method from *Wu and Peltier* [1984] shows the validity of the assumption $|s| \ll \sigma_0$. However, as mentioned in section 1, there is one problem with the method in [*Wu and Peltier*, 1984]: the loading itself is assumed to be stationary relative to the rotational axis and is not updated by the polar motion. For the case of TPW due to a mass anomaly which is shown in Figure 6, during the polar wander, the mass anomaly is calculated in the body-fixed coordinates, which means it is treated as being always located at 45° colatitude. However, when the rotation axis drifts away from the mass anomaly by 1°, in that instantaneous moment, the mass anomaly is actually placed at 46° colatitude. Of course, when only very small angle TPW is considered, the difference can be small but the exact effect has not been studied. We will show the magnitude of the error in the next section with a new method for calculating large-angle TPW.

3.2. Large-Angle Polar Wander

The limitation of the method in *Wu and Peltier* [1984] and the numerical method presented in the previous section is that they are based on the Liouville equation which is linearized at the position where the *z* axis of the coordinate system is the rotational axis and the equatorial bulge is perpendicular to this axis. As a result, this method cannot deal with large-angle TPW when the rotation axis drifts away from this position. However, if we assume that during the process of polar wander the equatorial readjustment is fast enough (or the polar wander is slow enough) so that the equatorial bulge is always nearly (but not necessarily exactly) perpendicular to the rotational axis, then we can define a new reference frame in which the new *z* axis coincides with the current rotational axis and we can linearize the Liouville equation in the new coordinate system. Physically, the process of TPW is the process of the rotational axis moving toward the axis of the maximum moment of inertia while the axis of the maximum moment of inertia is being pushed further away by the viscoelastic relaxation of the body and the displacement of the mass anomaly. What we assume is that the angle between these two axes is small enough so that the linearization of the Liouville equation is valid. This assumption is fundamentally different from assuming that during the TPW the rotational axis and the principle axis of the moment of inertia coincide [*Jurdy*, 1978; *Rouby et al.*, 2010; *Steinberger and O'Connell*, 1997]. The validity of this assumption is studied and discussed in detail in the study of *Cambiotti et al.* [2011] which develops, within the frame of a nonlinear approach for TPW induced by internal mass anomalies, a linear scheme of the Liouville equation in the system of the principal moments of inertia reference frame of the mass anomaly. Apparently, this assumption can be violated by a situation where the TPW is triggered by a very large mass anomaly which corresponds to an inertia tensor that is comparable in magnitude to the inertia tensor of the rotational body itself. In this case, the angle between the largest moment of inertia (the sum of the inertia tensors of both rotating body and the mass anomaly) and the rotational axis would be too large to apply the linearized Liouville equation. One advantage of our numerical method is that during the calculation, we can constantly monitor the validity of this assumption as will be shown by the end of this section. Generally, we can do a coordinate transformation in each step and apply the method we used for small angular change in the new coordinate system so that the local angular change in each step remains small enough.

We define the vector of the rotation as $\boldsymbol{\omega} = \Omega(\omega_1, \omega_2, \omega_3)^T$, where $(\omega_1, \omega_2, \omega_3)$ is a unit vector. For an arbitrary $\boldsymbol{\omega}$, the TPW which starts from this vector needs to be calculated in the frame whose *Z* axis coincides with $\boldsymbol{\omega}$. So we need to transform the original body-fixed coordinates into this new frame . The coordinate transformation matrix of a rotation from the vector $(0, 0, 1)$ to the unit vector $\boldsymbol{\omega}$ can be obtained from a general rotation matrix [*Arvo*, 1992] in which the third column of the matrix is $(\omega_1, \omega_2, \omega_3)^T$.

$$\mathbf{Q} = \begin{pmatrix} \omega_3 + \frac{\omega_2^2}{1+\omega_3} & -\frac{\omega_1\omega_2}{1+\omega_3} & \omega_1 \\ -\frac{\omega_1\omega_2}{1+\omega_3} & 1 - \frac{\omega_2^2}{1+\omega_3} & \omega_2 \\ -\omega_1 & -\omega_2 & \omega_3 \end{pmatrix} \tag{15}$$

For a centrifugally deformed body triggered by a mass anomaly which corresponds to the inertia tensor $\Delta\mathbf{I}_L$, the algorithm for calculating the large-angle TPW is as follows:

Algorithm 2

1. Assume that the step *i* starts at time t_i with the vector of the rotation being $\boldsymbol{\omega}^i = \Omega^i(\omega_1^i, \omega_2^i, \omega_3^i)$ and ends at time t_{i+1} with the vector of the rotation $\boldsymbol{\omega}^{i+1}$. For the first iteration, we assume that the vector of the rotation does not change: $\boldsymbol{\omega}^{i+1} = \boldsymbol{\omega}^i$.

2. Obtain $\Delta\mathbf{I}$ and its derivative $\Delta\dot{\mathbf{i}}$ from FEM or using equation (2) in the same way as step 2 in algorithm 1. With $\mathbf{Q}$ as defined in equation (15) being the coordinate transformation matrix from the body-fixed coordinates to the local coordinates where the Z axis aligns with the direction of the rotation, the inertia tensors in the transformed coordinates are obtained by $\Delta\mathbf{I}_1 = \mathbf{Q}^T\Delta\mathbf{I}\mathbf{Q}$ and $\Delta\dot{\mathbf{i}}_1 = \mathbf{Q}^T\Delta\dot{\mathbf{i}}\mathbf{Q}$.

3. Substitute $\Delta\mathbf{I}_1$ and $\Delta\dot{\mathbf{i}}_1$ into equation (11) and obtain $\boldsymbol{\omega}' = \Omega^i(m_1, m_2, 1 + m_3)^T$. We normalize this vector as $\boldsymbol{\omega}' = \Omega^{i+1}\bar{\boldsymbol{\omega}}'$ where $\bar{\boldsymbol{\omega}}'$ is the direction of the perturbed rotational axis in the local coordinate system and needs to be transformed back into the body-fixed frame to obtain $\boldsymbol{\omega}^{i+1} = \Omega^{i+1}\mathbf{Q}\,\bar{\boldsymbol{\omega}}'$ where Ω^{i+1} is the same as in the previous equation.

4. Substitute $\boldsymbol{\omega}^{i+1}$ into step 2 until the result converges.

There are two major differences between algorithms 1 and 2. First, in algorithm 2, the rotational perturbation is calculated in a transformed coordinate system instead of the original body-fixed frame in each step. Second, the initial load $\Delta\mathbf{I}_L$ is also updated in each step in response to the change of the rotational axis. As we can see in step 2 in algorithm 2, since $\Delta\mathbf{I}$ contains both the change in the moment of inertia due to deformation $\Delta\mathbf{I}_D$ and the initial load $\Delta\mathbf{I}_L$, we have $\mathbf{Q}^T\Delta\mathbf{I}\mathbf{Q} = \mathbf{Q}^T\Delta\mathbf{I}_D\mathbf{Q} + \mathbf{Q}^T\Delta\mathbf{I}_L\mathbf{Q}$. So $\mathbf{Q}^T\Delta\mathbf{I}_L\mathbf{Q}$ instead of $\Delta\mathbf{I}_L$ is used as the input for the driving factor of the TPW. In this way we lift the assumption of a stationary load as in *Wu and Peltier* [1984] and algorithm 1.

For validation purposes, we test if algorithm 2 can produce the same result as algorithm 1 for a small angle when we disable the updating of ΔI_L. This means in step 2 of algorithm 2, we only do a coordinate transform for the inertia tensor due to deformation but keep the one for the loading the same, so the total change for the inertia tensor is calculated as $\Delta\mathbf{I}_1 = \mathbf{Q}^T\Delta\mathbf{I}_D\mathbf{Q} + \Delta\mathbf{I}_L$ instead of $\Delta\mathbf{I}_1 = \mathbf{Q}^T(\Delta\mathbf{I}_D + \Delta\mathbf{I}_L)\mathbf{Q}$. Then the condition is the same as in *Wu and Peltier* [1984] and algorithm 1. To show the effect of the assumption of a stationary load, we also calculate the result with the original algorithm 2 (ΔI_L is updated). The comparison of the semi-analytical result from Wu, our numerical result without updating the loading and the numerical result with updated loading is shown in Figure 7. When the loading is not updated in each step, the numerical and the normal mode results show perfect agreement. This validates algorithm 2 as well as the assumption that the equatorial readjustment in this case is fast enough to catch up the polar wander. On the other hand, when the loading is updated in each step, as we can see in Figure 7, the normal mode result overestimates the TPW by about 2.5% for 2° of TPW. This is understandable, as the mass anomaly has its largest loading effect when it is at 45° (or 135°) colatitude. When the positive mass anomaly is attached at the surface at 60° colatitude, as the TPW proceeds, the mass anomaly moves toward the equator and the loading effect decreases. As a result, the speed of TPW slows down. Thus, with the method of *Wu and Peltier* [1984], depending on whether or not the TPW is displacing the mass anomaly toward or away from 45° latitude, the result can be either underestimated or overestimated, respectively. The bias becomes much larger if the mass anomaly is close to 0, 90, and 180° colatitude: If we place the same mass anomaly at 10° colatitude, after a polar wander of 2° the error can be up to 12 % with the stationary loading assumption. Consequently, the applicable range of the linear method becomes even smaller when the loading is close to poles or the equator. The comparison between the result from *Wu and Peltier* [1984] and the updated linear method (algorithm 2) is similar to that in the Figure 3 of *Sabadini and Peltier* [1981] which compares the TPW path on a homogeneous viscoelastic sphere from both a linear and nonlinear scheme. One apparent difference is the lack of an elastic response in the results of *Sabadini and Peltier* [1981]. Figure 8 shows how large the TPW can be as a function of colatitude in order to keep the error below 1.5%.

As can be derived from Figure 8, for the situation when the initial load is close to the pole or equator, the applicable range of the linear theory is quite limited. As a consequence, results obtained from linear rotation theory may need to be reconsidered for studies such as TPW on Earth driven by ice loss from Greenland or Antarctica, since these areas are close to the poles.

Next we test the behavior of our numerical method for large-angle polar wander and compare the result with the method of *Ricard et al.* [1993]. Ricard et al. assume that the Earth model has no internal nonadiabatic
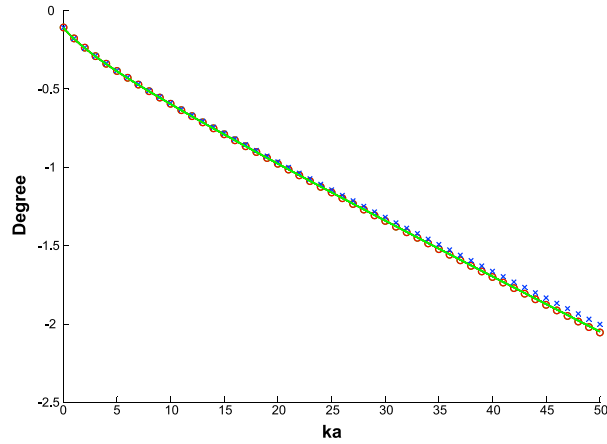
Figure 7. Polar wander in the *x-z* plane for the SG6 Earth model triggered by a point mass of 2×10^{19} kg attached at the surface at 60° colatitude. The line, red circles, and blue crosses represent the semianalytical result from *Wu and Peltier* [1984], our numerical result without updating loading, and the numerical result with updated loading, respectively.

density gradients (no M1 or M2 modes) and with $|s| << |s_i|$, the tidal Love number is approximated as

$$
\begin{aligned}
k^T(s) &= k_e^T + \sum_{i=1}^{M} \frac{k_i^T}{s - s_i} \\
&\approx k_e^T - \sum_{i=1}^{M} \frac{k_i^T}{s_i} \\
&= k_f^T(1 - T_1 s)
\end{aligned}
\tag{16}
$$

where k_e^T is the elastic Love number, k_i^T are the residues of each mode, and s_i are the inverse relaxation times. The time constant T_1 is

$$
T_1 = \frac{1}{k_f^T} \sum_{i=1}^{M} \frac{k_i^T}{s_i^2}
\tag{17}
$$

This assumption, which is called the quasi-fluid approximation, is actually the first-order approximation of the tidal Love number. It assumes that the relaxation time of every mode is much shorter than the time span for long-term polar wander. With this approximation, the nonlinear equation (1) can be simplified into a first-order
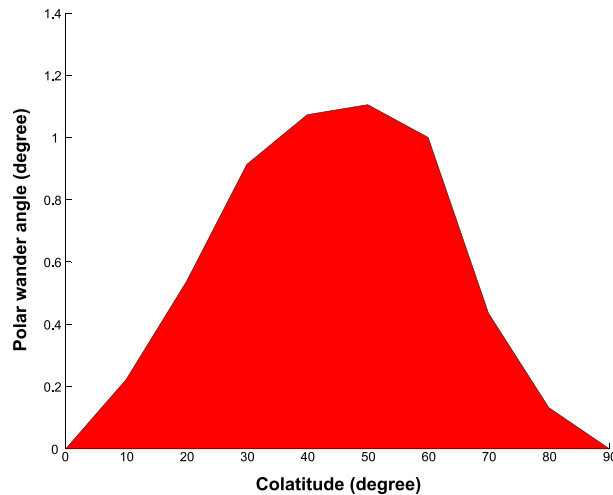

Figure 8. The allowed range of polar wander in order to obtain less than 1.5% error as a function of the colatitude of the loading.
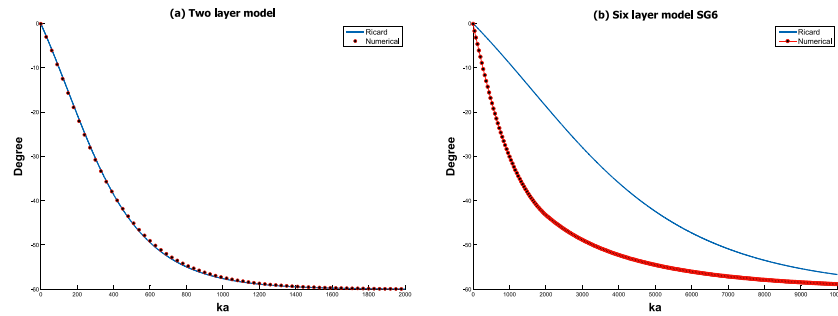
Figure 9. The polar wander in *x-z* plane of the two Earth models triggered by a point mass of 2×10^{19} kg placed at 30° colatitude in the *x-z* plane. Lines show the semianalytical results from *Ricard et al.* [1993], and symbols represent our numerical results (only half of the data points for the two-layer model and one tenth of the SG6 data points are shown in the figures).

differential equation for $\omega(t)$ and solved numerically. We first validate the accuracy of our numerical method by calculating TPW for the two-layer Earth model (Table 1). This is because a two-layer Earth model, which is a viscoelastic layer over a fluid core, does not contain the relatively slow modes (M1 and M2 modes). So the quasi-fluid approximation is reliable in this case and the TPW calculated by the method in *Ricard et al.* [1993] can be expected to be accurate. The comparison of our numerical and the semianalytical results for a two-layer model is shown in Figure 9a. As we can see, the two methods have very good agreement. Except for the first few points, where the difference is due to the elastic response that is missing in Ricard et al.'s results, the differences are below 0.5%.

Then we use both methods to calculate TPW for the six-layer SG6 model. This model approximates the real Earth better and also contains the slow M1 and M2 modes, which allows us to test the quasi-fluid approximation. The results are shown in Figure 9b. It is clear that for the SG6 model, the two methods show large differences and the polar wander given by *Ricard et al.* [1993] is much slower due to the lack of the relaxation from the M1 and M2 modes. To further validate our results and rule out the cause of numerical error, we also compare the semianalytical results from both *Wu and Peltier* [1984] and *Ricard et al.* [1993] for short-angle changes. As shown in Figure 10, we see again that in the two-layer model, despite the lack of the elastic response which gives the initial jump in Ricard et al.'s results, both results stay almost parallel. However, for the SG6 model, Ricard et al.'s results, which lack the contribution from M1 and M2 modes, lag behind from the beginning.
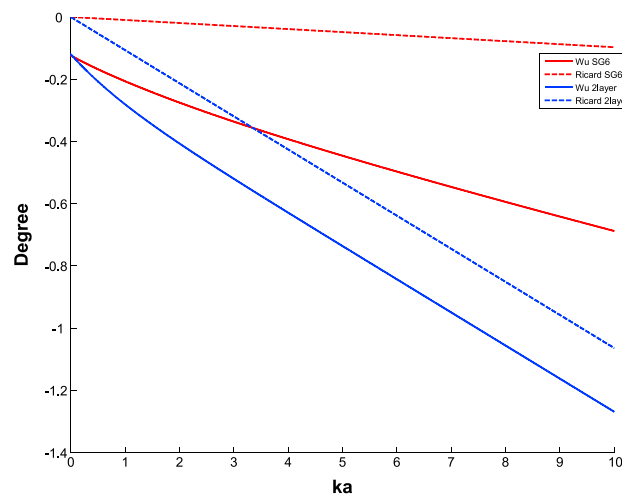

Figure 10. Polar wander in the *x-z* plane of the two Earth models triggered by a point mass of 2×10^{19} kg placed at 45° colatitude in the *x-z* plane, for two different semianalytical methods.

After long enough time results from *Ricard et al.* [1993] will converge to the same end position as the numerical one, but the large difference in transient behavior suggests that the quasi-fluid approximation is not a good choice for obtaining a time-dependent solution.

The numerical method we developed in this section is very general since the only assumption we take is that the equatorial readjustment is fast enough that the equatorial bulge is almost always perpendicular to the rotational axis. This means that the largest principle axis for the moment of inertia must nearly coincide with the rotational axis, so the inertia tensor in the coordinate system where the *Z* axis is the direction of the rotation is close to a diagonal matrix. We can check if this condition is satisfied during the

numerical calculation by comparing the diagonal elements in the inertial tensor with the nondiagonal ones: in the transformed coordinate system, the condition $\Delta I'_{ij}, i \neq j \ll \Delta I'_{ii}$ must be satisfied. Tests show that for TPW on two-layer Earth model with magnitudes of the mass anomalies below 2×10^{22} kg (this amount is about 100 times that of the ice sheets melted during the last deglaciation [*Ricard et al.*, 1993]), this condition is satisfied. Only when the model is driven by an even larger mass anomaly, this condition fails by a significant amount and the linear and nonlinear methods do not agree any more like in Figure 9a.

4. Reorientation of a Rotating Tidally Deformed Viscoelastic Body

As mentioned in section 1, *Willemann* [1984] and *Matsuyama and Nimmo* [2007] presented a solution which only calculates the final position of the reorientation. We are not aware of a general dynamic solution for the reorientation of a tidally deformed body. Two major difficulties prevent applying the existing rotation theory, linear or nonlinear, to a tidally deformed body. First, the principle inertia moments *A* and *B* are not equal in this case. Second, it is difficult to combine the effects of the centrifugal and tidal potential so that the deformed body and load can achieve the minimal potential state throughout the reorientation process. In the previous section we have already solved the first problem by deriving a more general linearized form of the Liouville equation (equation (11)). The main focus for the development of the method in this section is on how the tidal potential is treated and how the centrifugal and tidal potential can be combined.

When the reorientation of a tidally deformed body is studied, it is necessary that not only the rotational axis is considered but also the direction of the tidal axis which is the vector pointing to the central body. In this paper, we only consider the situation in which the rotational body is tidally locked in a circular orbit so the body is co-rotating with its central body and the direction of the tidal axis is always perpendicular to the rotational axis (the obliquity or axial tilt is zero).

For an incompressible model, the effective centrifugal potential is [*Murray and Dermott*, 2000]

$$\Phi_c = \frac{1}{3}\Omega^2 r^2 P_2^0(\cos\theta) \tag{18}$$

with θ being the colatitude and P_2^0 the associated Legendre function of degree 2, order 0. The tidal potential due to the central body at the same point can be written as [*Murray and Dermott*, 2000]

$$\Phi_t = -\frac{GM}{a^3}r^2 P_2^0(\cos\psi) \tag{19}$$

Here G, M, and a are the gravitational constant, the mass of the central body, and the radius of the orbit, respectively. ψ is the angle between the radius vector and the direction of the tidal bulge. Generally, if we define the equivalent angular speed of the tidal potential as

$$\Omega' = \sqrt{\frac{3GM}{a^3}} \tag{20}$$

then the form of the tidal potential becomes the same as the centrifugal potential except for the negative sign. When the rotational body is tidally locked in a circular orbit, then the rotational period is the same as the orbital period which is $T = 2\pi\sqrt{a^3/GM}$, from which it is easy to see that the magnitude of the tidal potential is always 3 times the magnitude of the centrifugal potential.

Because of the negative sign, the effect of applying a tidal potential to a certain object is the same as applying the centrifugal potential of the same magnitude but with opposite direction of the force. As a result, a positive mass anomaly driven by a centrifugal potential acts exactly like a negative mass anomaly driven by a tidal potential and vice versa. A centrifugal force always tries to relocate a positive mass anomaly to the equator and a negative mass anomaly to the poles to minimize the total potential, while a tidal potential tries to relocate the positive mass anomaly to the subhost point (the closest point on the body to the central body) or its antipodal and a negative mass anomaly to the great circle which is perpendicular to the direction of the tidal bulge. In order to calculate the change of the inertia tensor due to both the rotational and tidal potential, in FEM we need to add the tidal force to the model and apply equation (4). If equation (2) is used instead of the FE model, then we need to add an extra term for the contribution of the tidal potential. Since the effect of the tidal potential is exactly the same as the centrifugal potential except the direction, similar to the rotational vector, we can define a tidal vector which describes the strength and direction of the tidal force
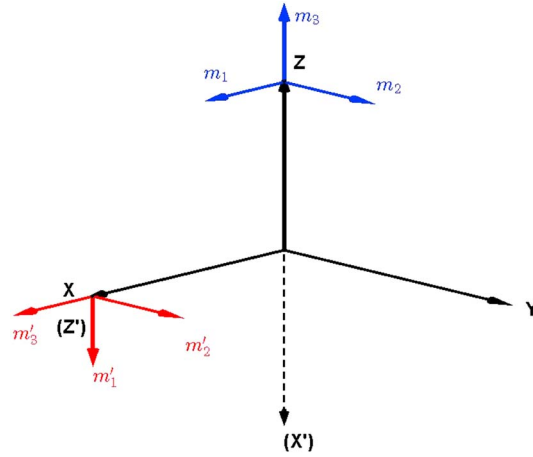
Figure 11. Bulge-fixed coordinate system where the X and Z axes are aligned with the direction of the tidal axis and the rotational axis, respectively. m_1, m_2, and m_3 correspond to the perturbation of the rotational axis. m'_1, m'_2, and m'_3 correspond to the perturbation of the tidal axis.

as $\mathbf{X} = \Omega'(\omega'_1, \omega'_2, \omega'_3)^T$, where Ω' is equivalent angular speed and $(\omega_1, \omega_2, \omega_3)^T$ is a unit vector. We have the perturbed inertia tensor due to tidal potential as

$$\Delta I_{T\_ij}(t) = -\frac{k^T(t)a^5}{3G} * \left(\Omega'^2 \left[\omega'_i(t)\omega'_j(t) - \frac{1}{3}\delta_{ij} \right] \right) \tag{21}$$

This term needs to be added to the right side of the equation (2). Notice the negative sign because in the case of the tidal potential, the direction of the force to the body is opposite to the centrifugal potential, so the perturbed inertia tensor is also negative.

In previous sections, the assumption was stated that the centrifugal potential is applied along the Z axis. Since the centrifugal force flattens the body, we have $C > A, B$. On the other hand, if we treat the tidal potential in the same way and apply it along the Z axis, the tidal force would elongate the body and we have $C < A, B$. For equation (11) to be valid, the conditions $C \neq A$ and $C \neq B$ are required. So we can use equation (11) to calculate the perturbation of both rotational and tidal axes. We define a moving bulge-fixed coordinate system in which the Z axis aligns with the direction of rotation and the X axis with the tidal bulge, as shown in Figure 11. In order to use equation (11), the direction of the tidal potential needs to be along the third axis of the coordinates (just as the rotation axis is along the Z axis of (X, Y, Z) frame). So the "polar" wander of the tidal axis is calculated in the coordinate system (X', Y, Z') where X' and Z' align with the negative Z and X axes, see Figure 11. The transformation matrix from (X, Y, Z) to (X', Y, Z') is written as

$$\mathbf{S} = \begin{pmatrix} 0 & 0 & -1 \\ 0 & 1 & 0 \\ 1 & 0 & 0 \end{pmatrix} \tag{22}$$

If the inertia tensor for both the triggering load and the deformation and its derivative is obtained in the (X, Y, Z) frame as $\Delta\mathbf{I}$ and $\Delta\dot{\mathbf{i}}$, these values are to be used to calculate the rotational axis change. Then the corresponding values for the tidal axis change are

$$\Delta\mathbf{I}_T = -\mathbf{S}^T\Delta\mathbf{I}\,\mathbf{S} \tag{23}$$

$$\Delta\dot{\mathbf{i}}_T = -\mathbf{S}^T\Delta\dot{\mathbf{i}}\,\mathbf{S} \tag{24}$$

$\Delta\mathbf{I}_T$ and $\Delta\dot{\mathbf{i}}_T$ are substituted into equation (11) to determine the local change of the tidal axis. When both the centrifugal and tidal potential are applied to the body perturbed by a certain load, as can be seen from Figure 11, the centrifugal force tries to relocate the rotational axis from $\mathbf{Z} = (0, 0, \Omega)^T$ to

$$\mathbf{Z}' = \Omega(m_1, m_2, 1 + m_3)^T \tag{25}$$

and the tidal force tries to push the tidal axis from $\mathbf{X} = (\Omega', 0, 0)$ to

$$\mathbf{X}' = \Omega' \left(1 + m'_3, m'_2, -m'_1\right)^T \tag{26}$$

Here Ω' is the equivalent angular speed defined by equation (20). The problem here is that these two conditions cannot be simultaneously satisfied since the new X and Z axes should also be perpendicular to each other because the feature of the tidal axis being orthogonal to the rotation axis does not change due to the reorientation. Considering that the X-Z plane is the one which constrains the directions of both rotational and tidal axes, this plane has to satisfy both conditions. So we have to make a compromise of the conditions: we let one of the axes, either X or Z, to be relocated at the exact desired location of equation (26) or (25) but the other one only lies within the new X-Z plane defined by vector $\mathbf{X}'$ and $\mathbf{Z}'$. Let $\bar{\mathbf{X}}'$ and $\bar{\mathbf{Z}}'$ be the normalized vectors of $\mathbf{X}'$ and $\mathbf{Z}'$, then we can calculate the new Y axis which is perpendicular to the X-Z plane as

$$\bar{\mathbf{Y}}' = \bar{\mathbf{Z}}' \times \bar{\mathbf{X}}' \tag{27}$$

Here $\times$ is the cross product. If we put the X axis at x, then the new Z axis which lies in the X-Z plane is determined as

$$\bar{\mathbf{Z}}'' = \bar{\mathbf{X}}' \times \bar{\mathbf{Y}}' \tag{28}$$

and the coordinate transformation matrix from the frame (X,Y,Z) to the frame (x_0, y_0, z'_0) is given by

$$\mathbf{V} = [\bar{\mathbf{X}}', \bar{\mathbf{Y}}', \bar{\mathbf{Z}}''] \tag{29}$$

Physically, the relocation of X and Z axes minimizes the total potential of the body and the initial mass anomaly related to the tidal and centrifugal force, respectively. Our method first achieves the minimization of the potential corresponding to one of the forces, then the other. When the relocation of X axis converges, then the change of the X axis becomes nearly 0, namely, $\bar{\mathbf{X}}' \approx (1, 0, 0)$. As a result, from equations (28) and (29), we have $\bar{\mathbf{Z}}'' \approx \bar{\mathbf{Z}}'$. So eventually, the minimal potential state associated with both the centrifugal and tidal force is found. This is similar to multiple-objective optimization [*Miettinen*, 1999]. Of course we can also first put the Z axis at $\mathbf{Z}'$ and then we calculate the new X axis as $\bar{\mathbf{X}}'' = \bar{\mathbf{Y}}' \times \bar{\mathbf{Z}}'$ and obtain the coordinate transform matrix $\mathbf{V} = [\bar{\mathbf{X}}'', \bar{\mathbf{Y}}', \bar{\mathbf{Z}}']$. Tests show that in either way, the results converge to the same final position of both rotational and tidal axes in each step.

For a tidally deformed body triggered by a certain mass anomaly which corresponds to inertia tensor $\Delta\mathbf{I}_L$, the complete algorithm for calculating the reorientation is given as follows:

Algorithm 3

1. Assume that the step i, from time t_i to t_{i+1}, starts with the direction of the rotational axis given by $\boldsymbol{\omega}_r^i = \Omega_r^i(\omega_1^i, \omega_2^i, \omega_3^i)^T$ and the direction of the tidal axis by $\boldsymbol{\omega}_t^i = \Omega_t^i(\omega_4^i, \omega_5^i, \omega_6^i)^T$ in which $(\omega_1^i, \omega_2^i, \omega_3^i)^T$ and $(\omega_4^i, \omega_5^i, \omega_6^i)^T$ are unit column vectors which satisfy $\omega_1^i\omega_4^i + \omega_2^i\omega_5^i + \omega_3^i\omega_6^i = 0$. Ω_t^i is the equivalent angular speed of the tidal potential calculated from equation (20). For the first iteration, we assume that the rotation and tidal axes in this step do not change: $\boldsymbol{\omega}_r^{i+1} = \boldsymbol{\omega}_r^i$ and $\boldsymbol{\omega}_t^{i+1} = \boldsymbol{\omega}_t^i$.
2. Apply both the centrifugal and tidal potential to the model in the same way as stated in step 2 in algorithm 1 to either FE model (equation (4)) or use equation (2) and add the term from equation (21). Obtain the total change in the inertia tensor and its derivative as $\Delta\mathbf{I}$ and $\Delta\dot{\mathbf{I}}$. The coordinate transformation matrix from the body-fixed to the bulge-fixed coordinate system is given by

$$\mathbf{U} = \left[\boldsymbol{\omega}_t^{i+1}, \boldsymbol{\omega}_r^{i+1} \times \boldsymbol{\omega}_t^{i+1}, \boldsymbol{\omega}_r^{i+1}\right] \tag{30}$$

   The local values of the inertia tensor for the centrifugal part are obtained by $\Delta\mathbf{I}_1 = \mathbf{U}^T\Delta\mathbf{I}\,\mathbf{U}$ and $\Delta\dot{\mathbf{I}}_1 = \mathbf{U}^T\Delta\dot{\mathbf{I}}\,\mathbf{U}$. The corresponding inertia tensors for calculating tidal perturbation are $\Delta\mathbf{I}_2 = -\mathbf{S}^T\Delta\mathbf{I}_1\,\mathbf{S}$ and $\Delta\dot{\mathbf{I}}_2 = -\mathbf{S}^T\Delta\dot{\mathbf{I}}_1\,\mathbf{S}$
3. Apply equation (11) to $\Delta\mathbf{I}_1$ and $\Delta\dot{\mathbf{I}}_1$ and obtain the perturbation for the rotational axis as $\Omega_1(m_1, m_2, m_3)$. Apply equation (11) to $\Delta\mathbf{I}_2$ and $\Delta\dot{\mathbf{I}}_2$ and obtain the perturbation for the tidal axis as $\Omega_2(m'_1, m'_2, m'_3)$. Then we have the perturbed Z and X axis as $\mathbf{Z}' = \Omega_1(m_1, m_2, 1 + m_3)^T$ and $\mathbf{X}' = \Omega_2(1 + m'_3, m'_2, -m'_1)^T$. We normalize these vectors as $\mathbf{Z}' = \Omega_r^{i+1}\bar{\mathbf{Z}}'$ and $\mathbf{X}' = \Omega_t^{i+1}\bar{\mathbf{X}}'$. The local coordinate transformation matrix from

Table 3. Properties of Triton

Layer	Outer Radius (km)	Density (kg m^{-3})	Shear Modulus (Pa)	Viscosity (Pa s)
Ice I	1352	937	3.6×10^9	1×10^{21}
Ice II	1100	1193	6.2×10^9	1×10^{21}
Mantle	950	3500	65×10^9	1×10^{19}
Core	600	5844.8	0	0

the bulge-fixed frame at time t_i to the new frame at time t_{i+1} is obtained as $\mathbf{V} = [\bar{\mathbf{X}}', \bar{\mathbf{Z}}' \times \bar{\mathbf{X}}', \bar{\mathbf{X}}' \times (\bar{\mathbf{Z}}' \times \bar{\mathbf{X}}')]$. The updated direction of the rotational and tidal axes in the original body-fixed coordinates are obtained as

$$\boldsymbol{\omega}_r^{i+1} = \Omega_r^{i+1} \mathbf{UV}[0, 0, 1]^T \tag{31a}$$

$$\boldsymbol{\omega}_t^{i+1} = \Omega_t^{i+1} \mathbf{UV}[1, 0, 0]^T \tag{31b}$$

4. Substitute $\boldsymbol{\omega}_r^{i+1}$ and $\boldsymbol{\omega}_t^{i+1}$ in step 2 until the results converge.

In order to show how the reorientation of a tidally deformed rotating body is accomplished, we choose a model of Triton, the largest moon of Neptune. Triton is an icy moon and tidally locked. It has zero obliquity and small orbital eccentricity which is about 1.6×10^{-5} and can be ignored, so it fits the situation of our assumption. The interior structure is chosen according to the empirical model presented in *Spohn et al.* [2014] which fits observations of Triton's mass and moment of inertia. Depending on the amount of internal heating, there can be an ocean between the high pressure and low pressure ice [*Spohn et al.*, 2014]. For simplicity, the effect of a possible ocean is ignored. The physical properties of the model are shown in Table 3.

To trigger the reorientation, a surface mass anomaly with a magnitude of 3.6×10^{17} kg, either positive or negative, is chosen. This amount is approximately the accumulation of nitrogen snow during 10,000 years which is sublimated from the equatorial area, then moves to the polar areas where it is deposited [*Rubincam*, 2003]. We simulate the polar wander of Triton for two cases: (1) a positive mass anomaly at high latitude (20° colatitude) and (2) a negative mass anomaly at low latitude (60° colatitude). In each case, the mass anomaly is placed at three different longitudes: -15, -45, and $-75°$. Due to the symmetry, only situations in one quadrant are considered. The initial loading time T_0 and the time span for the TPW are both chosen to be 4 million years at which, from normal mode method, the time history of the tidal Love number reaches about 99.75% of its fluid Love number, following equation (12). With this range of time, the reorientation should be close to its equilibrium position. In order to better describe the three types of the reorientation as shown in Figure 1, in the bulge-fixed frame we define the reorientation of the tidal deformed rotating body around the Z, X, and Y axes as the Z reorientation, X reorientation, and Y reorientation, respectively. The results for the cases of positive mass anomalies are shown in Figures 12 and 13.
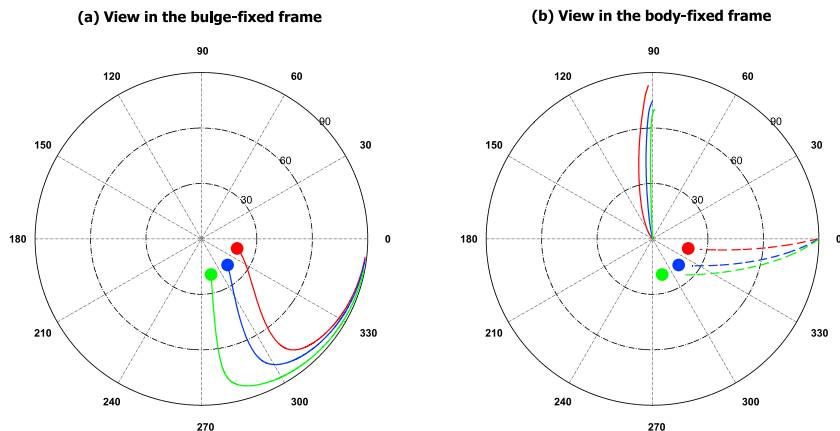

Figure 12. Reorientation caused by positive mass anomalies placed at 20° colatitude, -15, -45, and -75 longitudes. (a) The traces (lines) of the positive mass anomalies (filled circles) in the bulge-fixed frame where the sub-Neptune point is at 0° longitude. (b) The traces of the north pole of Triton (lines) and sub-Neptune point (dashed lines) in the body-fixed frame.
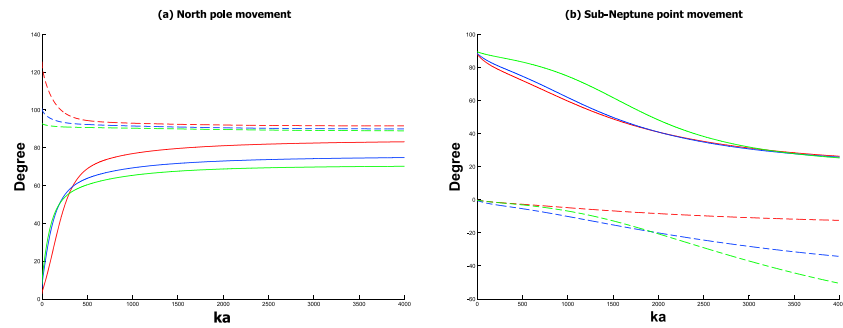
Figure 13. Reorientation caused by positive mass anomalies placed at 20° colatitude, −15, −45, and −75° longitudes. The time history for the colatitudes (solid lines) and longitudes (dashed lines) of the north pole. (b) The time history for the colatitudes (solid lines) and longitudes (dashed lines) of the sub-Neptune point.

Figure 12a gives the paths of the mass anomalies in the bulge-fixed coordinates. We can see that when the positive mass anomaly is placed at high colatitude, the reorientation first pushes the mass anomalies toward the equator with an X reorientation. When the mass anomaly is close to the equator, a Z reorientation follows and eventually the mass anomaly tries to reach the sub-Neptune point. Due to the Z reorientation, in the body-fixed coordinates as shown in Figure 12b, the pole does not drift away from the mass anomalies in a straight line; instead, it moves closely along the great circle which is perpendicular to the tidal axis. This is different compared to the case of polar wander on a centrifugally deformed body such as Earth. From Figures 13a and 13b, by comparing the speed of the pole in colatitude direction and that of the subhost point in longitudinal direction, we can see that the X reorientation is much faster than the Z reorientation. This indicates that it is much easier to reorient the tidal bulge around the tidal axis than the rotational axis. So the direction of the polar wander due to unbalanced ice caps on Triton is more likely to go around the tidal axis instead of going toward it. As a result, the suggestion that the direction of the polar wander for the viscoelastic case of Triton would be toward the sub-Neptune point when the reorientation starts [*Rubincam*, 2003] does not seem to be correct.

Cases of negative anomalies are shown in Figures 14 and 15. These cases apply to situations like the south polar terrain of Enceladus, in which *Nimmo and Pappalardo* [2006] suggests that the diapirism of the lower density material creates a negative mass anomaly which is relocated to the south pole due to the reorientation of Enceladus. In contrast with the case of positive mass anomaly, we see in Figure 14a that the reorientation has a slight preference to first push the mass anomaly to the great circle where both tidal and rotational axes are located or to the 0 and 180 degree longitude circle. This indicates that the Z reorientation is slightly faster than the Y reorientation, so the direction of both rotational and tidal axes are still not directly targeting their end positions. Figures 15a and 15b shows that except for the case where the negative mass anomaly is
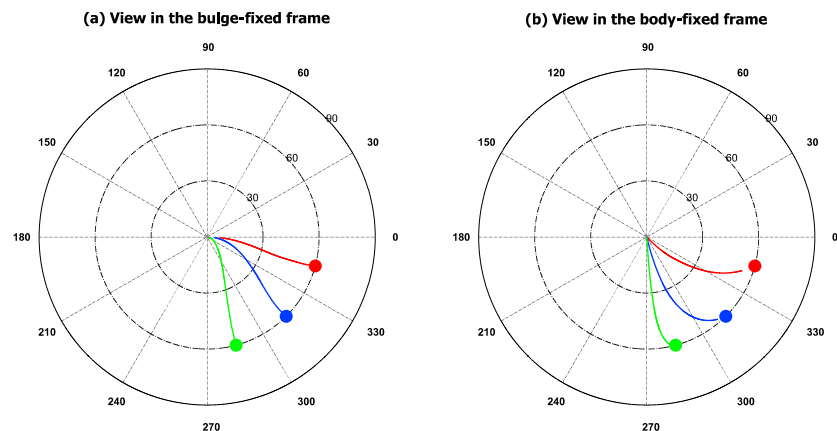

Figure 14. Reorientation cased by negative mass anomalies placed at 60° colatitude, −15, −45, and −75 longitudes. The traces (lines) of the negative mass anomalies (filled circles) in the bulge-fixed frame where the sub-Neptune point is at 0° longitude. The traces of the north pole (lines) in the body-fixed frame.
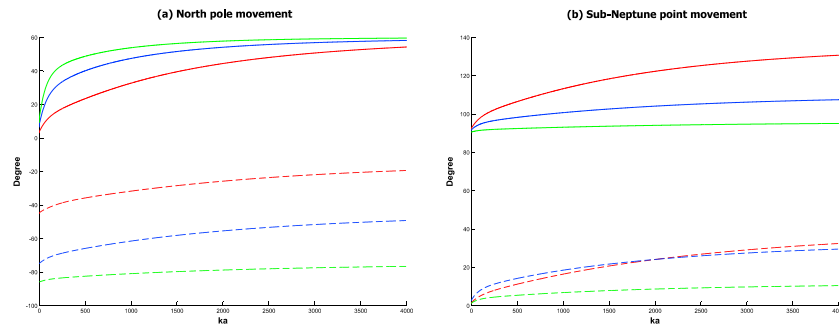
Figure 15. Reorientation cased by negative mass anomalies placed at 60° colatitude, −15, −45, and −75° longitudes. The time history for the colatitudes (solid lines) and longitudes (dashed lines) of the north pole and the time history for the colatitudes (solid lines) and longitudes (dashed lines) of the sub-Neptune point.

close to the ±90 longitude (case with the green color), there is no drastic speed change. This is quite different compared to cases with positive anomalies which always begin with a relatively fast X reorientation.

From both cases of positive and negative anomalies, we see that for a tidally deformed rotating body, the X reorientation is much faster than the Z reorientation, while the Z reorientation is slightly faster than the Y reorientation. Such preference for the direction of the reorientation can be explained in the following way. Since the tidal potential is larger than the centrifugal potential, diagonal elements of the inertia tensor in the bulge-fixed frame satisfies $A < B < C$ and $C - B < B - A$. The rotation of the same small angle around X, Y, and Z axes changes the diagonal inertia tensor $\mathbf{I}$ into $\mathbf{Q}_i^T \mathbf{I} \mathbf{Q}_i$, where $\mathbf{Q}_i$, $i = 1, 2, 3$, are the transformation matrices for rotations around X, Y, and Z axes. These transformations produce nondiagonal elements with magnitude ΔI_{23}, ΔI_{13}, and ΔI_{12}, respectively, and it is easy to prove that they have the relation: $\Delta I_{23} < \Delta I_{12} < \Delta I_{13}$. These cross products represent the resistance of the bulge, either rotational or tidal, against the polar (tidal) wander, so the reorientation around the X axis is the fastest while that around the Y axis is the slowest. From the track of both positive and negative mass anomaly in various positions shown in Figures 12 and 14, we can also conclude that except for the six dead zones where both centrifugal and tidal force are either very small or in equilibrium (the areas around the poles, the subhost point and its antipode, and the two points facing the orbit), positive mass anomalies are more likely to be found around the equator and the great circle perpendicular to the tidal axis while negative mass anomalies tend to be around the 0 and 180° longitude great circle in the bulge-fixed frame.

It is also worth to mention that our method can be extended to situations where the obliquity or orbit eccentricity is nonzero. In these cases, we need to change the transformation matrix $\mathbf{S}$ given by equation (22), which would become time dependent and needs to be updated according to the position of the body in the orbit and the relative location of the rotational and tidal axes in each step of the numerical calculation.

5. Conclusions

Numerical methods for calculating both small- and large-angle reorientation of a centrifugally and tidally deformed viscoelastic body are established. The methods are validated by comparing with existing normal mode methods which were developed for both small-angle and large-angle TPW. With the help of the developed numerical methods, the following conclusions can be drawn:

1. Linear rotation theory leads to a bias which can be very large when the initial position of the mass anomaly causing the true polar wander (TPW) is close to the poles or equator. This significantly limits the applicable range of the linear method if loads are close to poles or equator.
2. The time-dependent result of TPW obtained by taking the first-order approximation of the tidal love number, namely, the quasi-fluid approximation, gives large errors for the transient behavior and only when the model is close to its final orientation, results taking quasi-fluid approximation give reliable prediction. This makes quasi-fluid approximation not a good choice for studying transient viscoelastic readjustment of Earth or other planets which contain significant slow relaxation modes.
3. A tidally deformed body has a preference of the reorientation around the tidal axis over that around the rotational axis. The rotational axis driven by a positive mass anomaly near the poles tends to first rotate around the tidal axis instead of toward it. For tidally locked bodies which do not have a remnant bulge,

positive mass anomalies are more likely to be found around the equator and the great circle perpendicular to the tidal axis, while negative mass anomalies tend to be near the great circle that contains the tidal and rotational axes.

Appendix A

Since the results from the FEM are validated by comparing with the analytical results obtained from a normal mode method which is based on Maxwell rheology, the material properties need to be defined in FEM such that the viscoelastic response of the material is equivalent to that of a Maxwell material. In the Abaqus FEM package, the viscoelastic property of the material is defined in the following way: (1) the initial elasticity is defined separately by giving the Young's modulus in the option "Elasticity." (2) the normalized viscoelastic behavior can be defined either with the "Creep" option which uses power law strain-hardening or a "Viscoelastic" option which uses the Prony series which is a general scheme that encompasses a simple Maxwell rheology. In Abaqus, Prony series expansion is defined by the dimensionless relaxation modulus g_R as

$$g_R(t) = 1 - \sum_{i=1}^{N} g_i^P (1 - e^{-t/\tau_i^G}) \tag{A1}$$

where N, g_i^P, and τ_i^G are material constants. As the equivalence of Maxwell rheology, we have $N = 1$, $g_1^P = 1 - 1^{-10}$ (Abaqus requires that $g_i^P < 1$, so a value very close to 1 is chosen) and $\tau_1^G = \mu/E$ where μ and E are material viscosity and elasticity.

Both options give similar results with the same accuracy for the time history of the tidal Love number or the individual components of the inertia tensor (Figure 3). However, when the terms which determine the TPW (like in Figure 4) are calculated, which are the combinations of the components of the inertia tensor, the results obtained with the Creep option, as can be seen in Figure A1, show a much larger error compared to those obtained with the option Viscoelastic as shown in Figure 4. This demonstrates that the Viscoelastic option in Abaqus is a better choice to represent a Maxwell material. This suggests that also comparisons between results from Abaqus and spectral models [*Wu and van der Wal*, 2003; *van der Wal et al.*, 2015] might be improved.
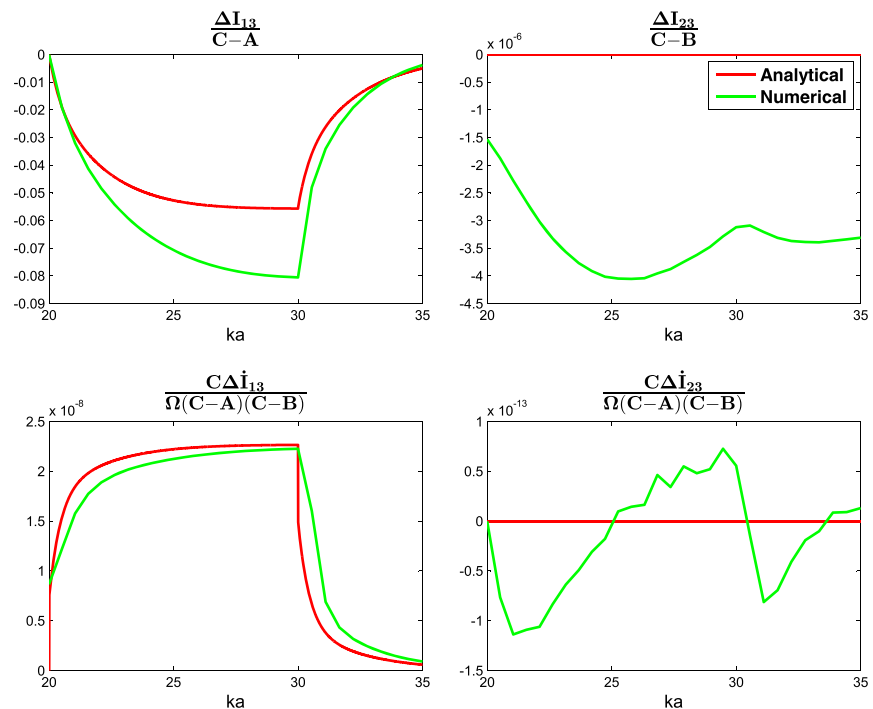

Figure A1. Result of the same test as that in Figure 4 with the viscous deformation being defined with the option Creep in Abaqus.

References

Arvo, J. (1992), *Graphics Gems III*, chap. Fast Random Rotation Matrices, Academic Press Professional, Inc., pp. 117–120, San Diego, Calif.

Cambiotti, G., Y. Ricard, and R. Sabadini (2010), Ice age true polar wander in a compressible and non-hydrostatic Earth, *Geophys. J. Int.*, *183*(3), 1248–1264, doi:10.1111/j.1365-246x.2010.04791.x.

Cambiotti, G., Y. Ricard, and R. Sabadini (2011), New insights into mantle convection true polar wander and rotational bulge readjustment, *Earth Planet. Sci. Lett.*, *310*(3), 538–543.

Chan, N.-H., J. X. Mitrovica, A. Daradich, J. R. Creveling, I. Matsuyama, and S. Stanley (2014), Time-dependent rotational stability of dynamic planets with elastic lithospheres, *J. Geophys. Res. Planets*, *119*(1), 169–188.

Farrell, W. E. (1972), Deformation of the Earth by surface loads, *Rev. Geophys.*, *10*(3), 761–797.

Gold, T. (1955), Instability of the Earth's axis of rotation, *Nature*, *175*(4456), 526–529.

Harada, Y. (2012), Long-term polar motion on a quasi-fluid planetary body with an elastic lithosphere: Semi-analytic solutions of the time-dependent equation, *Icarus*, *220*(2), 449–465.

Hinderer, J., H. Legros, and M. Amalvict (1982), A search for Chandler and nearly diurnal free wobbles using Liouville equations, *Geophys. J. Int.*, *71*(2), 303–332.

Jurdy, D. (1978), An alternative model for early tertiary absolute plate motions, *Geology*, *6*(1), 469.

Malcuit, R. (2014), *The Twin Sister Planets Venus and Earth: Why are they so different?*, Springer Link: Bücher, Springer International Publishing, Switzerland.

Matsuyama, I., and F. Nimmo (2007), Rotational stability of tidally deformed planetary bodies, *J. Geophys. Res.*, *112*, E11003, doi:10.1029/2007JE002942.

Matsuyama, I., J. X. Mitrovica, A. Daradich, and N. Gomez (2010), The rotational stability of a triaxial ice-age Earth, *J. Geophys. Res.*, *115*, B05401, doi:10.1029/2009JB006564.

Miettinen, K. (1999), *Nonlinear Multiobjective Optimization*, International Series in Operations Research and Management Science, pp. 37–57, Springer.

Mitrovica, J. X., and J. Wahr (2011), Ice age Earth rotation, *Annu. Rev. Earth Planet. Sci.*, *39*(1), 577–616.

Mitrovica, J. X., J. Wahr, I. Matsuyama, and A. Paulson (2005), The rotational stability of an ice-age Earth, *Geophys. J. Int.*, *161*(2), 491–506.

Munk, W., and G. MacDonald (1960), *The Rotation of the Earth: A Geophysical Discussion*, Cambridge Monographs on Mechanics and Applied Mathematics, Cambridge Univ. Press, Cambridge.

Murray, C., and S. Dermott (2000), *Solar System Dynamics*, Cambridge Univ. Press, Cambridge.

Nakada, M. (2002), Polar wander caused by the quaternary glacial cycles and fluid love number, *Earth Planet. Sci. Lett.*, *200*(1), 159–166.

Nakiboglu, S. M., and K. Lambeck (1980), Deglaciation effects on the rotation of the Earth, *Geophys. J. R. Astron. Soc.*, *62*(1), 49–58.

Nimmo, F., and R. T. Pappalardo (2006), Diapir-induced reorientation of Saturn's Moon Enceladus, *Nature*, *441*(7093), 614–616.

Ojakangas, G. W., and D. J. Stevenson (1989), Polar wander of an ice shell on Europa, *Icarus*, *81*(2), 242–270.

Peltier, W. R., and X. Jiang (1996), Glacial isostatic adjustment and Earth rotation: Refined constraints on the viscosity of the deepest mantle, *J. Geophys. Res.*, *101*(B2), 3269–3290.

Ricard, Y., G. Spada, and R. Sabadini (1993), Polar wandering of a dynamic Earth, *Geophys. J. Int.*, *113*(2), 284–298.

Rouby, H., M. Greff-Lefftz, and J. Besse (2010), Mantle dynamics, geoid, inertia and TPW since 120 Myr, *Earth Planet. Sci. Lett.*, *292*(3), 301–311.

Rubincam, D. P. (2003), Polar wander on Triton and Pluto due to volatile migration, *Icarus*, *163*(2), 469–478.

Sabadini, R., and W. R. Peltier (1981), Pleistocene deglaciation and the Earth's rotation: Implications for mantle viscosity, *Geophys. J. R. Astron. Soc.*, *66*(3), 553–578.

Sabadini, R., and B. Vermeersen (2004), *Global Dynamics of the Earth: Applications of Normal Mode Relaxation Theory to Solid-Earth Geophysics*, Modern Approaches in Geophysics, Springer, Netherlands.

Schultz, P. H., and A. B. Lutz (1988), Polar wandering of Mars, *Icarus*, *73*(1), 91–141.

Spada, G., Y. Ricard, and R. Sabadini (1992), Excitation of true polar wander by subduction, *Nature*, *360*(6403), 452–454.

Spada, G., R. Sabadini, and E. Boschi (1996), Long-term rotation and mantle dynamics of the Earth, Mars, and Venus, *J. Geophys. Res.*, *101*(E1), 2253–2266.

Spohn, T., D. Breuer, and T. Johnson (2014), *Encyclopedia of the Solar System*, pp. 861–882, Elsevier Science, Amsterdam.

Steinberger, B., and R. J. O'Connell (1997), Changes of the Earth's rotation axis owing to advection of mantle density heterogeneities, *Nature*, *387*(6629), 169–173, doi:10.1038/387169a0.

Šrámek, O., and S. Zhong (2012), Martian crustal dichotomy and Tharsis formation by partial melting coupled to early plume migration, *J. Geophys. Res.*, *117*, E01005, doi:10.1029/2011JE003867.

van der Wal, W., P. L. Whitehouse, and E. J. Schrama (2015), Effect of GIA models with 3D composite mantle viscosity on GRACE mass balance estimates for Antarctica, *Earth Planet. Sci. Lett.*, *414*, 134–143.

Vermeersen, L. L. A., and R. Sabadini (1996), Significance of the fundamental mantle rotational relaxation mode in polar wander simulations, *Geophys. J. Int.*, *127*(2), F5–F9.

Wang, H., P. Wu, and W. van der Wal (2008), Using postglacial sea level, crustal velocities and gravity-rate-of-change to constrain the influence of thermal effects on mantle lateral heterogeneities, *J. Geodyn.*, *46*, 104–117, doi:10.1016/j.jog.2008.03.003.

Willemann, R. J. (1984), Reorientation of planets with elastic lithospheres, *Icarus*, *60*, 701–709.

Wu, P. (2004), Using commercial finite element packages for the study of Earth deformations, sea levels and the state of stress, *Geophys. J. Int.*, *158*(2), 401–408.

Wu, P., and W. R. Peltier (1984), Pleistocene deglaciation and the Earth's rotation: A new analysis, *Geophys. J. R. Astron. Soc.*, *76*(3), 753–791.

Wu, P., and W. van der Wal (2003), Postglacial sealevels on a spherical, self-gravitating viscoelastic Earth: Effects of lateral viscosity variations in the upper mantle on the inference of viscosity contrasts in the lower mantle, *Earth Planet. Sci. Lett.*, *211*(1), 57–68.